Published in final edited form as:
Angew Chem Int Ed Engl. 2019 October 14; 58(42): 15005–15009. doi:10.1002/anie.201909686.

A Nontrigonal Tricoordinate Phosphorus Ligand Exhibiting Reversible 'Nonspectator' L/X–Switching

Gregory T. Cleveland[a], **Alexander T. Radosevich***,[a]

[a]Department of Chemistry, Massachusetts Institute of Technology, 77 Massachusetts Avenue, Cambridge, Massachusetts, 02139

Abstract

We report here a 'nonspectator' behavior for an unsupported L-function σ^3–P ligand (i.e. P{N[*o*-NMe-C_6H_4]$_2$}, **1a**) in complex with the cyclopentadienyliron dicarbonyl cation (Fp^+). Treatment of **1a**•Fp^+ with [$(Me_2N)_3S$][Me_3SiF_2] results in fluoride addition to the *P*-center, giving the isolable crystalline fluorometallophosphorane **1a^F**•Fp that allows a crystallographic assessment of the variance in the Fe–P bond as a function of *P*-coordination number. The nonspectator reactivity of **1a**•Fp^+ is rationalized on the basis of electronic structure arguments and by comparison to trigonal analogue $(Me_2N)_3P$•Fp^+ (i.e. **1b**•Fp^+), which is inert to fluoride addition. These observations establish a nonspectator L/X-switching in (σ^3–P)–M complexes by reversible access to higher-coordinate phosphorus ligand fragments.

Graphical Abstract

An L-function trivalent phosphorus ligand accepts fluoride ion by nucleophilic addition to generate a stable, isolable metallophosphorane; the reaction is reversible. Changes to the metal–phosphorus bonding as a function coordination number at P are analyzed crystallographically and computationally.

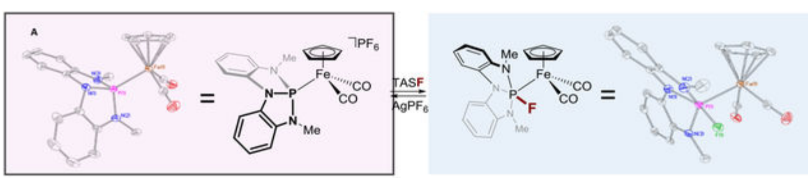

Keywords

coordination modes; hypervalent compounds; ligand effects; ligand reactivity; phosphorous ligands

---

Tricoordinate phosphorus (σ^3–P) compounds are archetypal donor ligands in coordination chemistry.[1,2,3] Within the Covalent Bond Classification,[4,5] σ^3–P compounds are designated L-function ligands for transition metals (M) and are overwhelmingly construed as inert, ancillary, spectator ligands within (σ^3–P)–M complexes. A rich 'nonspectator' reaction

---

radosevich@mit.edu.

chemistry of metal-bound σ^3–P compounds, however, belies this prevailing view. Abstraction of a *P*-substituent from (σ^3–P)–M complexes accesses dicoordinate phosphorus ligands (Figure 1a; σ^2–P^-, phosphide; σ^2–P^+, phosphenium),[6] and the σ^2–$P^{+/-}$/σ^3–P interconversion has been the focus of extensive stoichiometric[7,8,9,10,11,12,13] and catalytic[14] investigation. By complement, addition of an exogenous nucleophile to phosphorus in an L-function (σ^3–P)–M complex increases the *P*-coordination number, resulting in a 'metallophosphorane' complex with an X-function (σ^4–P)–M formula.[15] Literature concerning the addition of a *P*-substituent to (σ^3–P)–M complexes to give higher-coordinate phosphorus congeners is comparatively sparse.[16] Verkade has postulated that fluoride addition to Pd^{II}-(bis)phosphines induces $Pd^{II}\rightarrow Pd^0$ reduction via initial addition of F^- to P.[17] Further, Nakazawa and Miyoshi have shown the possibility of nucleophilic substitution of *P*-substituents in cationic Fe^{II}-phosphite complexes, in some cases leading to persistent (σ^4–P)–M products.[18,19]

Recently, a κ^3-chelate containing a nontrigonal σ^3–P center (Figure 1,B) was shown to access directly a (σ^4–P)–M metallophosphorane by formal insertion to a Ru–H bond.[20] An interpretation of XANES data for **B** and related compounds **A** attributed the propensity of the phosphorus center to attain higher coordination to the presence of a low-energy *P*-based orbital made accessible by the nontrigonal local environment.[21] The presence of the low-lying *P*-centered orbital in **A** and related compounds raised the prospect of accentuated intermolecular electrophilic reactivity of such nontrigonal σ^3–P ligands. We report here the reversible addition of an exogenous nucleophile to the *P*-center of an unsupported (σ^3–P)–M complex **C** that demonstrates a nonspectator behavior of ligands **A**. With this study, direct experimental evidence is provided that delineates: (1) the inherent electronic impact on metal-binding arising from nontrigonal distortion of σ^3–P ligands without convolution from chelate effects, and (2) the direct crystallographic observation of a nonspectator phosphorus ligand in a higher-coordination state following exogenous nucleophile addition. The ability for nontrigonal σ^3–P ligands to reversibly expand local coordination number while remaining σ-bound in the primary ligand sphere of a metal complex forecasts emerging opportunities for functional nonspectator ligands within (σ^3–P)–M complexes.2[2]

On the basis of precedent from Martin[23] and Nakazawa and Miyoshi,[18,19] the cyclopentadienyliron dicarbonyl cation (Fp^+) was selected as a coordinatively saturated 'ancillary metal'[24] fragment for study. Iron complexes **1a**•Fp^+ and **1b**•Fp^+ were prepared by ligand exchange of [thf•Fp][PF_6][25] with P{N[*o*-NMe-C_6H_4]$_2$} (**1a**)[26,27] and $(Me_2N)_3P$ (**1b**), respectively (Figure 2).

According to IR spectroscopy, the CO stretching frequencies of **1a**•Fp^+ (ν_{asym} 2017 cm^{-1}, ν_{sym} 2061 cm^{-1}) are higher in energy than those of **1b**•Fp^+ (ν_{asym} 2000 cm^{-1}, ν_{sym} 2045 cm^{-1}). This trend tracks qualitatively with the J_{Se-P} coupling constants for phosphorus selenides **1a**•Se (J_{Se-P} = 907 Hz) and **1b**•Se (J_{Se-P} = 784 Hz), suggesting to a first approximation that **1a** is a weaker σ-donor than **1b** (see Table 1 for collected metrical data). The ^{57}Fe NMR chemical shifts (obtained indirectly by 2D Fe–P correlation solution NMR experiments due to the low receptivity of the ^{57}Fe nucleus[28]) for **1a**•Fp^+ (δ 616 ppm) and **1b**•Fp^+ (δ 688 ppm) are consistent with this interpretation, based on trends established for related cyclopentadienyliron complexes.[29]

Further distinctions between **1a**•Fp^+ and **1b**•Fp^+ are manifest in structural analyses based on X-ray diffractometry data obtained with single-crystalline samples (Figure 3). Most evidently, compound **1a**•Fp^+ features a shorter Fe–P bond length ($d_{Fe–P}$ = 2.1809(4) Å) as compared to compound **1b**•Fp^+ ($d_{Fe–P}$ = 2.2381(5) Å). Also, consistent with the aforementioned vibrational data, the average Fe–C_{CO} bond length in **1a**•Fp^+ ($d_{Fe–C}$ = 1.7886(17) Å) is slightly longer than in **1b**•Fp^+ ($d_{Fe–C}$ = 1.7766(19) Å). A further feature of note concerns the dihedral angles φ(N-P-Fe-N); by projection down the P–Fe axis (Figure 3A, *right*), compound **1a**•Fp^+ shows a span of dihedral angles Ω(φ) = 28.11(26)°, with a maximum dihedral of φ(N_2-P-Fe-N_3) = 137.95(13)°. By contrast, compound **1b**•Fp^+ shows only a span of dihedral angles Ω(φ) = 5.3(3)° and a maximum dihedral of φ(N_1-P-Fe-N_3) = 121.87(14)°. These metrics illustrate the enhanced nontrigonal local geometry about phosphorus for **1a**•Fp^+ as compared to **1b**•Fp^+, consistent with the structural distinctions between the free ligands.[26] For reference, the N_2–P–N_3 bond angle of **1a**•Fp^+ (116.40(7)^0) is almost unchanged from that of **1a** (115.21(7)^0), showing that complexation does not significantly perturb the phosphorus triamide framework.

In an effort to parse the **σ**- and **π**- contributions to the Fe–P bonding interactions in **1a**•Fp^+ and **1b**•Fp^+, an energy partitioning into pairwise orbital interactions between σ^3–P ligand (**1a** and **1b**, respectively) and Fp^+ fragments was undertaken with the Energy Decomposition Analysis – Natural Orbitals for Chemical Valence (EDA-NOCV) method[30] as implemented in the ADF modeling program[31] at the BP86/def2-TZVP level of density functional theory (Table 1, see SI for full details). Along lines described by Michalak,[32] deconvolution of the covalent bonding portion (E_{orb}) into **σ**- and **π**-symmetry components for **1a**•Fp^+ gives donation σ(P→Fe) = −61.7 kcal/mol (65.9% of E_{orb}) and back-donation π(P←Fe) = −18.1 kcal/mol (19.3% of E_{orb}). An illustration of the electron deformation densities for the three principal NOCV interactions of **1a**•Fp^+ is presented in Figure 4. NOCV deformation density channel $\Delta\rho_1$ depicts depletion of electron density at P (red) and accrual of electron density at Fe (blue) as would be expected for an L-function **σ**-dative interaction. NOCV deformation density channels $\Delta\rho_2$ and $\Delta\rho_3$ correspond to the backflow of electron density from an Fe $d\pi$ orbital into *P*-based **π**-acceptor orbitals with two distinct interaction energies (ΔE^2_{orb} = −10.7 kcal/mol, ΔE^3_{orb} = −7.35 kcal/mol), consistent with the lifting of $p\pi$ degeneracy at nontrigonal **1a** shown by previous XAS evidence.[21] By way of comparison, EDA-NOCV partitioning of the Fe–P bond in **1b**•Fp^+ gives donation σ(P→Fe) = −65.8 kcal/mol (70.8% of E_{orb}) and back-donation π(P←Fe) = −13.2 kcal/mol (14.2% of E_{orb}). This analysis therefore quantifies the relatively weaker **σ**-donating ability of nontrigonal σ^3–P compound **1a** as compared to a compositionally related phosphorous triamide **1b** evident from spectroscopy (*vide supra*). Further, a combined consideration of the spectroscopic, structural, and theoretical data suggests a relatively stronger **π**-accepting ability of **1a** vs. **1b**.

To quantify the relative electrophilicity of *P*-based acceptor orbitals for **1a**•Fp^+ vs. **1b**•Fp^+, solvation-corrected fluoride ion affinities (FIAs) were computed at the M06L/def2-TZVP(CPCM:CH_2Cl_2) level of theory by isodesmic reaction enthalpies according to Christe's method.[33] The FIA for **1a**•Fp^+ is computed to be significantly larger (–ΔH = 59.3 kcal/mol) than that for **1b**•Fp^+ (–ΔH = 32.9 kcal/mol). The low absolute values for the FIAs are indicative a modest overall fluoride affinity,[34] but the difference Δ(FIA) = 26.4 kcal/mol conforms to the interpretation that *P*-based electrophilic reactivity should be favored at the nontrigonal complex **1a**•Fp^+.

The reactivity of **1a**•Fp^+ and **1b**•Fp^+ toward fluoride addition was probed experimentally. Treatment of compound **1a**•Fp^+ with tris(dimethylamino)sulfonium trimethyldifluorosilicate (TASF) in acetonitrile resulted in an immediate change in color from yellow to deep orange (Figure 5a). The formation of a single new phosphorus-containing species was evident by ^{31}P NMR spectroscopy, as indicated by the doublet resonance at δ −3.0 ppm, which displayed large scalar coupling (J = 971 Hz) consistent with the presence of a single fluorine bound to phosphorus via a direct P–F bond. The large upfield shift in ^{31}P NMR chemical shift is consistent with an increased coordination number at phosphorus by fluoride addition, and this inference is confirmed by observation of the complementary coupling in the lone ^{19}F NMR resonance (δ 27.4 ppm, J = 971 Hz, Figure 5b). The product was thus assigned to be fluorometallophosphorane $\mathbf{1a^F}$•Fp, in which a fluoride has been added to the phosphorus of **1a**•Fp^+ to generate a neutral complex. In solution, compound $\mathbf{1a^F}$•Fp exhibits time-averaged molecular C_s-symmetry with a persistent P–Fe bond; ^{13}C NMR spectra demonstrate an equivalence of the CO ligands (one resonance at δ 211 ppm) with well-resolved $^2J_{C–P}$ = 49 Hz and $^3J_{C–F}$ = 5.7 Hz coupling constants. Treatment of **1b**•Fp^+ to identical fluorinating conditions (TASF, MeCN, rt) does not result in fluorination but instead returns starting materials alongside some decomposition of **1b**•Fp^+. It is evident that fluoride addition to a higher coordinate phosphorus ligand is enabled by the enhanced electrophilicity of **1a**•Fp^+ as compared to **1b**•Fp^+.

The air and moisture sensitive orange $\mathbf{1a^F}$•Fp can be crystallized by slow evaporation of a saturated CH_2Cl_2 solution at −35° C (Figure 5c). X-ray diffractometry confirms the structural assignment of $\mathbf{1a^F}$•Fp as a metallophosphorane resulting from addition of an exogenous fluoride to σ^3–P ligand **1a** without further substitution. With respect to the Fe bonding environment, compound $\mathbf{1a^F}$•Fp features an increased Fe–P bond length ($d_{Fe–P}$ = 2.3047(9) Å) as compared to **1a**•Fp^+, as well as a shorter average Fe–C_{CO} bond length ($d_{Fe–C}$ = 1.764(3) Å) that coincides with a bathochromic shift of the carbonyl stretching frequencies (ν_{asym} 1952 cm^{-1}, ν_{sym} 2007 cm^{-1}). With respect to the P bonding environment, metrical parameters give a geometry index of τ = 0.35, indicating a geometry closer to that of a square pyramid than a trigonal bipyramid.[35] The addition of fluoride results in an increase in all of the P–N bond lengths by 0.05 Å < $\Delta d_{P–N}$ < 0.09 Å as is common for higher-coordinate main group compounds that compensate for their formal 'hypervalent' character by distribution of electron density toward the substituents.[36] The P–F bond length is quite long ($d_{P–F}$ = 1.6687(18) Å), but falls within the range (1.64(11) Å < $d_{P–F}$ < 1.69(1) Å) observed for the only prior example of a structurally characterized fluorometallophosphorane (i.e. $Ir(CO)Cl_2(PEt_3)_2(PF_4)$) from Holloway.[37]

Bonding analysis in **1a**•Fp^+ and $\mathbf{1a^F}$•Fp reveals changes to the nature of the Fe–P σ-interactions as a function of fluoride binding. NBO analysis reports a dative covalent P→Fe σ-interaction for **1a**•Fp^+ described by an NLMO comprising modest polarization toward the phosphorus (P 56.2%/Fe 38.5%; Figure 6a, *left*) and involving a P donor NBO with $sp^{1.10}$ hybridization. The NLMO corresponding to the P–Fe bonding interaction in $\mathbf{1a^F}$•Fp indicates an increased distribution across Fe–P (P 49.8%/Fe 43.9%; Figure 6b, *left*) with similar phosphorus parentage (*sp*$^{1.16}$). Moving from **1a**•Fp^+ to **1a^F**•Fp, the Wiberg bond indices decrease (**1a**•Fp^+: WBI = 0.53; **1a^F**•Fp: WBI = 0.48), in line with the observed increase in bond length from crystallography ($\Delta d_{P–Fe}$ = +0.12 Å). For comparison, similar qualitative trends are reported by Gabbai for addition of fluoride to antimony in Pt-Sb bimetallics.[38] Here, we invoke a decreased importance of π-backbonding effects in **1a^F**•Fp to account for this observation; the *P*-based acceptor orbital is saturated by addition of exogenous fluoride and unavailable for metal bonding.

Topological analysis of the computed electron density within the Quantum Theory of Atoms in Molecules (QTAIM) framework[39] returns bond paths defined by (3, −1) critical points for P–Fe in **1a**•Fp^+ (Figure 6a, *right*), and both P–Fe and P–F in **1a^F**•Fp (Figure 6b, *right*). No bond paths were located for any F…Fe or N…Fe trajectory, conforming to an η^1-formulation of metallophosphorane **1a^F**•Fp. Qualitatively, *P*-based valence shell charge concentrations are evident in the Laplacian of the electron density for both **1a**•Fp^+ and **1a^F**•Fp along the P–Fe bond path, in line with an L- and X-function ligand classification, respectively. By contrast, the Laplacian distribution for the P–F bond is indicative of a 'closed-shell interaction' and a dominant ionic contribution to the P–F bonding in **1a^F**•Fp.

Consistent with the ionic character of the P–F bonding interaction, treatment of **1a^F**•Fp with fluoride abstracting reagents leads to removal of the F^- ligand and regeneration of **1a**•Fp^+. Specifically, the addition of 1 equiv of $AgPF_6$ to a CD_3CN solution of **1a^F**•Fp induces the orange solution to become yellow with immediate formation of precipitate. Following filtration, ^{31}P NMR spectroscopy (Figure 5b) confirms full consumption of **1a^F**•Fp and clean return of compound **1a**•Fp^+. Evidently, both the nontrigonal phosphorus framework and the P–Fe bond are sufficiently robust as to be retained during the course of the nonspectator L→X→L-switching cycle.

The data reported herein define the spectroscopic, structural, and electronic changes that accrue to phosphorus ligand **1a** as it undergoes increase in coordination number upon exogenous fluoride addition. The conversion from L- to X- function roles results in little change to the donor capacity of the phosphorus ligand, but the acceptor capacity is diminished. Further, the reversible nonspectator behavior of tricoordinate phosphorus ligand **1a** calls to mind recent developments for higher valent states of Sb ligands from Gabbaï.[22] Given this periodic relationship within group 15, the broader implications of nonspectator L/X switching for phosphorus-based ligands in catalysis and sensing warrant further investigation.

Supplementary Material

Refer to Web version on PubMed Central for supplementary material.

Acknowledgements

Financial support was provided by NIH NIGMS (R21 GM134240). G.T.C. was supported by an NSF Graduate Research Fellowship. We thank Dr. Clemens Anklin (Bruker) for assistance with ^{57}Fe NMR studies. We thank Drs. Charlene Tsay and Peter Müeller (MIT) for assistance in crystallographic data collection.

References

[1]. Tolman CA, Chem. Rev 1977, 77, 313–348.

[2]. Crabtree RH, The Organometallic Chemistry of the Transition Metals. John Wiley and Sons, Inc, 2005, 87–124.

[3]. Gillespie JA, Zuidema E, van Leeuwen PWNM, Kamer PCJ, Phosphorus(III) Ligands in Homogenous Catalysis: Design and Synthysis. John Wiley and Sons, Inc, 2012, 1–26.

[4]. Green MLH, J. Organomet. Chem 1995, 500, 127–148.

[5]. Parkin G, in Comprehensive Organometallic Chemistry III, Volume 1, Chapter 1; Crabtree RH, and Mingos DMP, (Eds), Elsevier, Oxford, 2006.

[6]. Rosenberg L, Coord. Chem. Rev 2012, 256, 606–626.

[7]. Roddick DM, Santarsiero BD, Bercaw JE, J. Am. Chem. Soc 1985, 107, 4670–4678.

[8]. Fryzuk MD, Bhangu K, J. Am. Chem. Soc 1988, 110, 961–963.

[9]. Derrah EJ, Pantazis DA, McDonald R, Rosenberg L, Organometallics 2007, 26, 1473–1482.

[10]. Hoyle M-AM, Pantazis DA, Burton HM, McDonald R, Rosenberg L, Organometallics 2011, 30, 6458–6465.

[11]. Kim Y-E, Oh S, Kim S, Kim O, Kim J, Han SW, Lee Y, J. Am. Chem. Soc 2015, 137, 4280–4283. [PubMed: 25798737]

[12]. Oh S, Kim S, Lee D, Gwak J, Lee Y, Inorg. Chem 2016, 55, 12863–12871. [PubMed: 27989162]

[13]. Oh S, Lee Y, Organometallics 2016, 35, 1586–1592.

[14]. Poitras AM, Knight SE, Bezpalko MW, Foxman BM, Thomas CM, Angew. Chem. Int. Ed 2018, 57, 1497–1500.

[15]. Goodman J, Macgregor SA, Coord. Chem. Rev 2010, 254, 1295–1306.

[16]. Nakazawa H, Kubo K, Miyoshi K, Bull. Chem. Soc. Jpn 2001, 74, 2255–2267.

[17]. McLaughlin PA, Verkade JG, Organometallics 1998, 17, 5937–5940.

[18]. Kubo K, Nakazawa H, Mizuta T, Miyoshi K, Organometallics 1998, 17, 3522–3531.

[19]. Kubo K, Bansho K, Nakazawa H, Miyoshi K, Organometallics 1999, 18, 4311–4316.

[20]. Tanushi A, Radosevich A, J. Am. Chem. Soc 2018, 140, 8114–8118 [PubMed: 29923715]

[21]. Lee K, Blake AV, Tanushi A, McCarthy SM, Kim D, Loria SM, Donahue CM, Spielvogel KD, Keith JM, Daly SR, Radosevich AT, Angew. Chem. Int. Ed 2019, 58, 6993–6998.

[22]. For examples of high-valent heavier pnictogen ligands in catalysis and sensing, see:(a)Jones JS, Gabbaï FP, Acc. Chem. Res 2016, 49, 857–867. [PubMed: 27092722] (b)Jones JS, Wade CR, Gabbaï FP, Angew. Chem. Int. Ed, 2014, 53, 8876–8879.(c)You D, Gabbaï FP, J. Am. Chem. Soc 2017, 139, 6843–6846. [PubMed: 28485973] (d)You D, Yang H, Sen S, Gabbaï FP, J. Am. Chem. Soc 2018, 140, 9644–9651. [PubMed: 29979870]

[23]. Chopra SK, Martin JC, Heteroat. Chem 1990, 2, 71–79.

[24]. Boone MP, Stephan DW, Organometallics, 2014, 33, 387–393.

[25]. Catheline D, Astruc D, Organometallics 1984, 3, 1094–1100.

[26]. Zhao W, McCarthy SM, Lai TY, Yennawar HP, Radosevich AT, J. Am. Chem. Soc 2014, 136, 17634–17644. [PubMed: 25401723]

[27]. Lin Y-C, Hatzakis E, McCarthy SM, Reichl KD, Lai TY, Yennawar HP, Radosevich AT, J. Am. Chem. Soc 2017, 139, 6008–6016. [PubMed: 28398750]

[28]. Benn R, Brenneke H, Frings A, Lehmkuhl H, Mehler G, Rufinska A, Wildt T, J. Am. Chem. Soc 1988, 110, 5661–5668.

[29]. Mampa RM, Fernandes MA, Carlton L, Organometallics 2014, 33, 3283–3299.

[30]. For recent overviews of EDA-NOCV, see:(a)Frenking G, Bickelhaupt FM, The EDA Perspective of Chemical Bonding In The Chemical Bond; John Wiley & Sons, Ltd, 2014, 121–157.(b)Zhao L, von Hopffgarten M, Andrada DM, Frenking G, WIREs Comput. Mol. Sci 2018, 8, e1345.

[31]. ADF2018, SCM, Theoretical Chemistry, Vrije Universiteit, Amsterdam, The Netherlands, http://www.scm.com.

[32]. Mitoraj MP, Michalak A, Inorg. Chem 2010, 49, 578–582. [PubMed: 20014798]

[33]. Christe KO, Dixon DA, McLemore D, Wilson WW, Sheehy JA, Boatz JA J. Fluorine Chem 2000, 101, 151–153.

[34]. Slattery JM, Hussein S, Dalton Trans 2012, 41, 1808–1815. [PubMed: 22159000]

[35]. Addison AW, Rao TN, Reedijk J, van Rijn J, C Verschoor G, J. Chem. Soc. Dalt. Trans 1984, 1, 1349–1356.

[36]. Crabtree RH, Chem. Soc. Rev 2017, 46, 1720–1729. [PubMed: 28240328]

[37]. Blake AJ, Cockman RW, Ebsworth EAV, Henderson SGD, Holloway JH, Pilkington NJ, Rankin DWH, Phosphorus and Sulfur 1987, 30, 143–146.

[38]. Jones JS, Wade CR, Gabbaï FP, Organometallics 2015, 34, 2647–2654.

[39]. Bader R Atoms in Molecules: A Quantum Theory; Oxford University Press: Oxford, 1990.

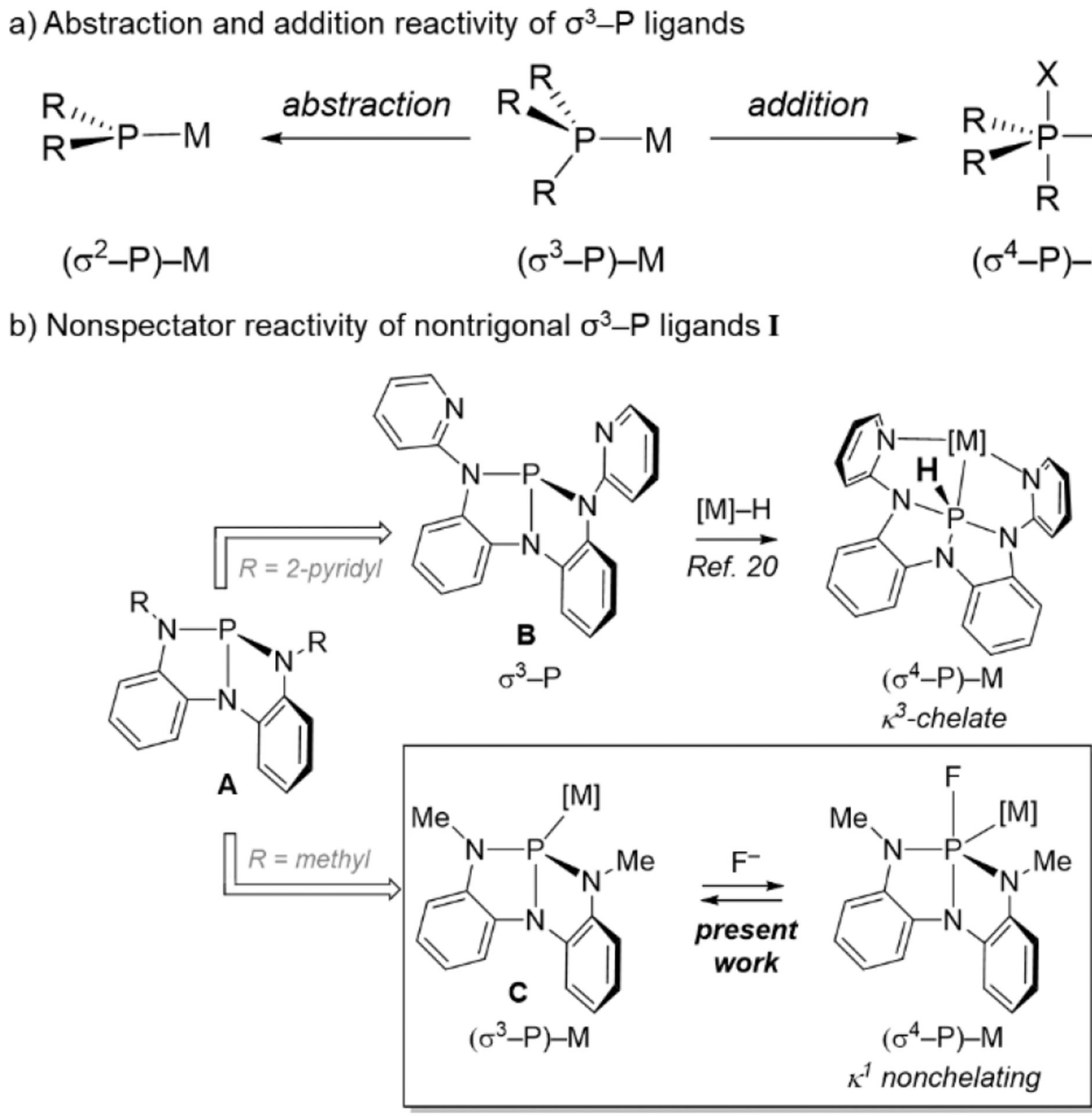

Figure 1.
Nonspectator modes of reactivity for (σ^3–P)–M complexes.

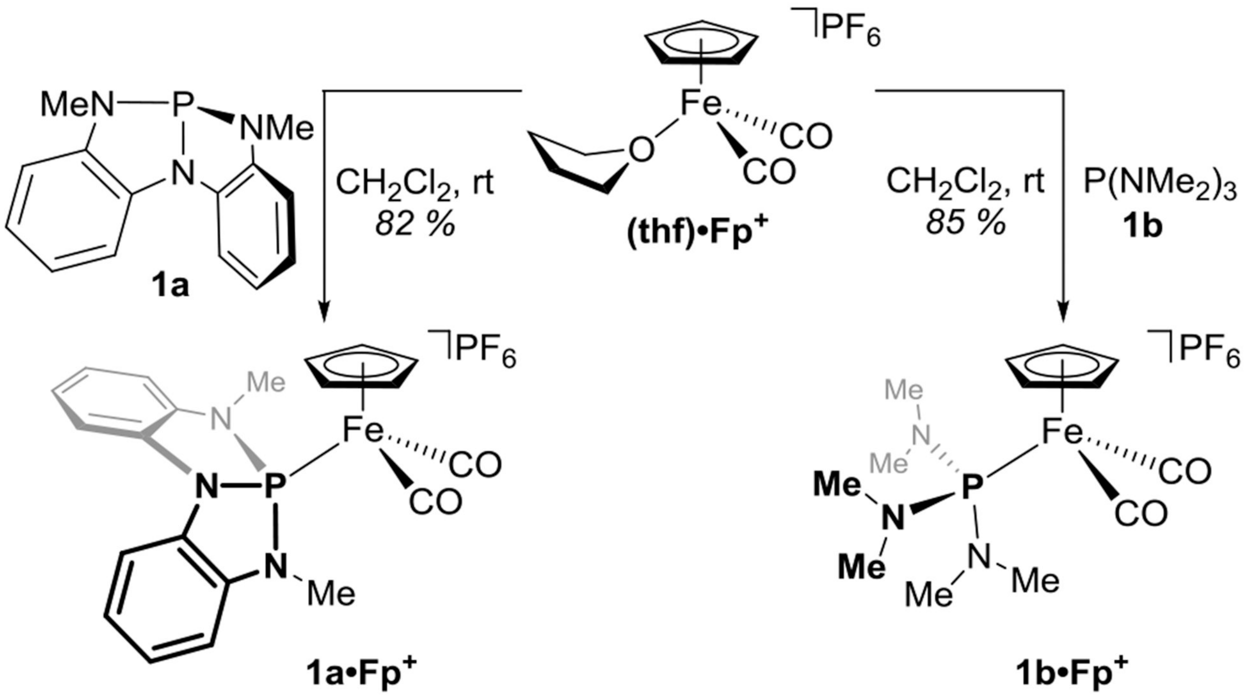

Figure 2.

Synthesis of [R_3P•Fp][PF_6] complexes, where R_3P = **1a** or **1b**.

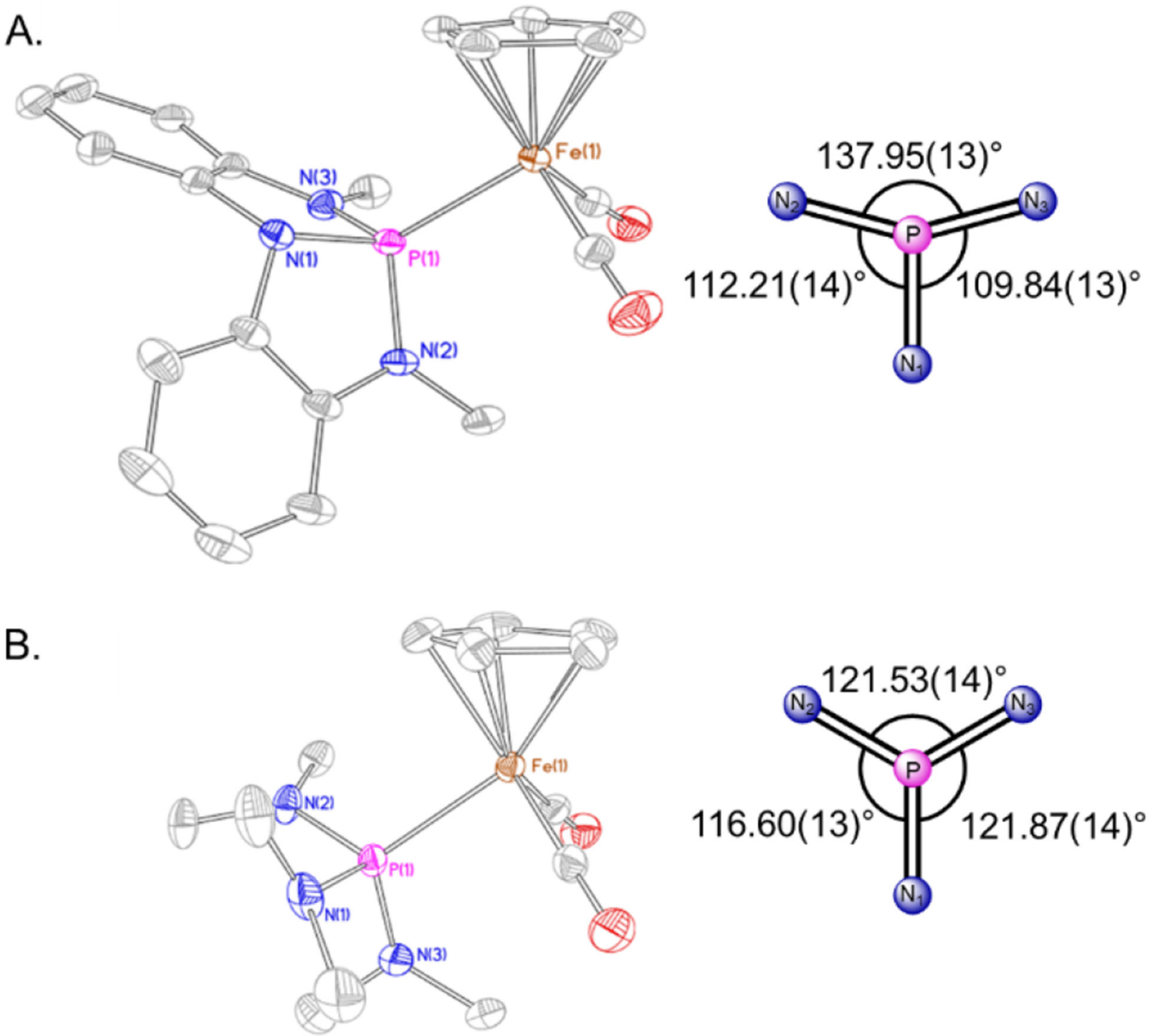

Figure 3.

(**A**) *Left:* Thermal ellipsoid plot for **1a**•Fp^+ rendered at 50% probability level. Hydrogen atoms, noncoordinating PF_6^- counterion, and a THF solvent molecule are omitted for clarity. Selected metrical data for **1a**•Fp^+: d(Fe-P): 2.1809(4) Å, d(Fe-$(CO)_1$): 1.7879(17) Å, d(Fe-$(CO)_2$): 1.7893(16) Å, ∠(N_1-P-N_2): 93.42(6)^o, ∠(N_1-P-N_3): 93.04(7)^o, ∠(N_2-P-N_3): 116.39(7)^o. *Right*: Schematic projection down the P–Fe axis for **1a**•Fp^+ illustrating dihedral angles φ(N-P-Fe-N). (**B**) *Left:* Thermal ellipsoid plot for **1b**•Fp^+ rendered at 50% probability level. Only one of two molecules in the asymmetric unit is depicted. Hydrogen atoms and a noncoordinating PF_6^- counterion are omitted for clarity. Selected metrical data for **1b**•Fp^+: d(Fe-P): 2.2381(5) Å, d(Fe-$(CO)_1$): 1.7739(19) Å, d(Fe-$(CO)_2$): 1.7792(18) Å, ∠(N_1-P-N_2): 101.59(8) ^{o}, ∠(N_1-P-N_3): 105.03(9)^o, ∠(N_2-P-N_3): 107.09(9)^o. *Right*: Schematic projection down the P–Fe axis for **1b**•Fp^+ illustrating dihedral angles φ(N-P-Fe-N). See SI for full details.

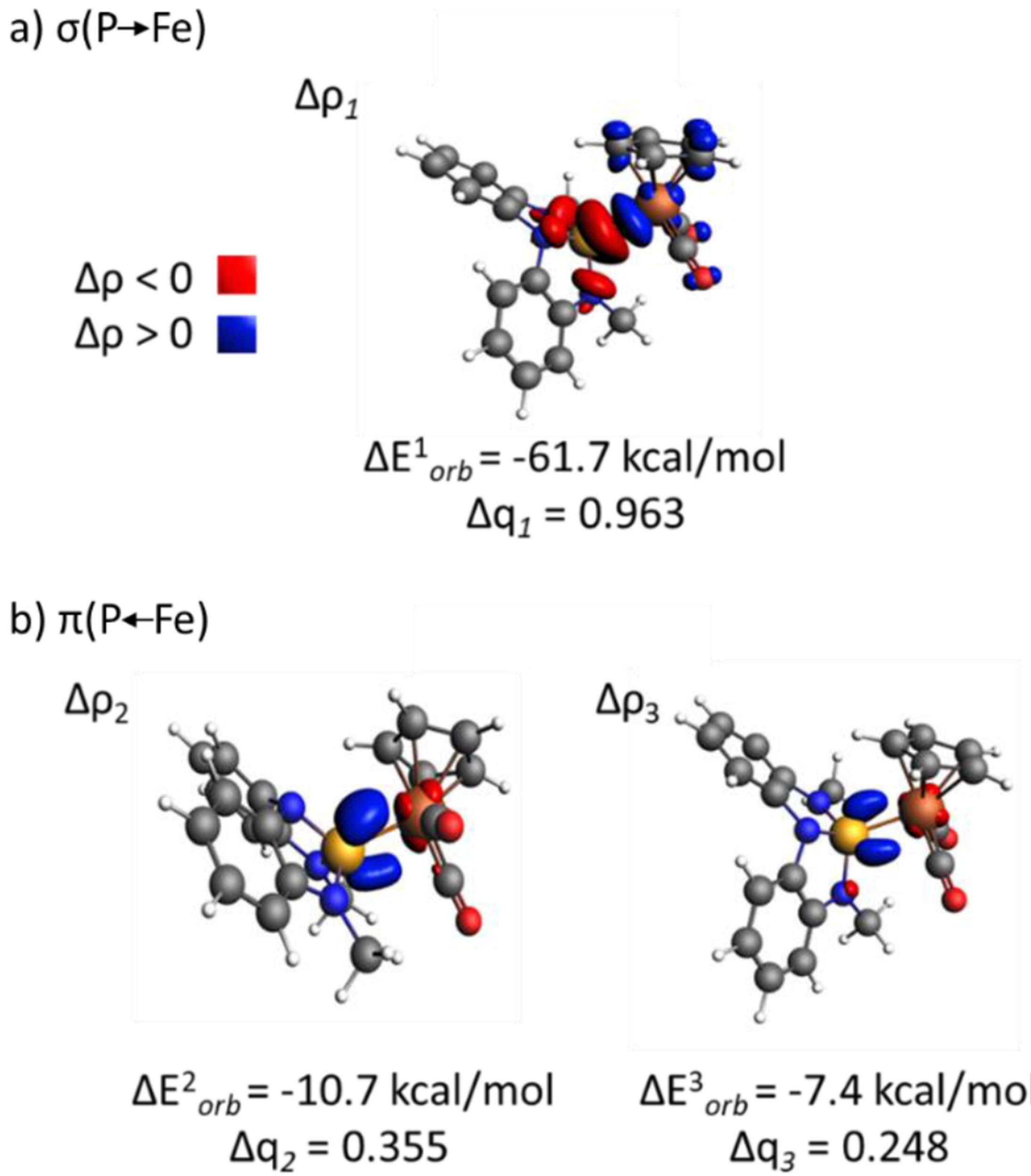

Figure 4.

Contours of electron deformation density channels $\Delta\rho_1$, $\Delta\rho_2$, and $\Delta\rho_3$ describing the bonding between **1a** and the Fp^+ metal fragments with corresponding energies and charge estimations obtained from EDA-NOCV method.

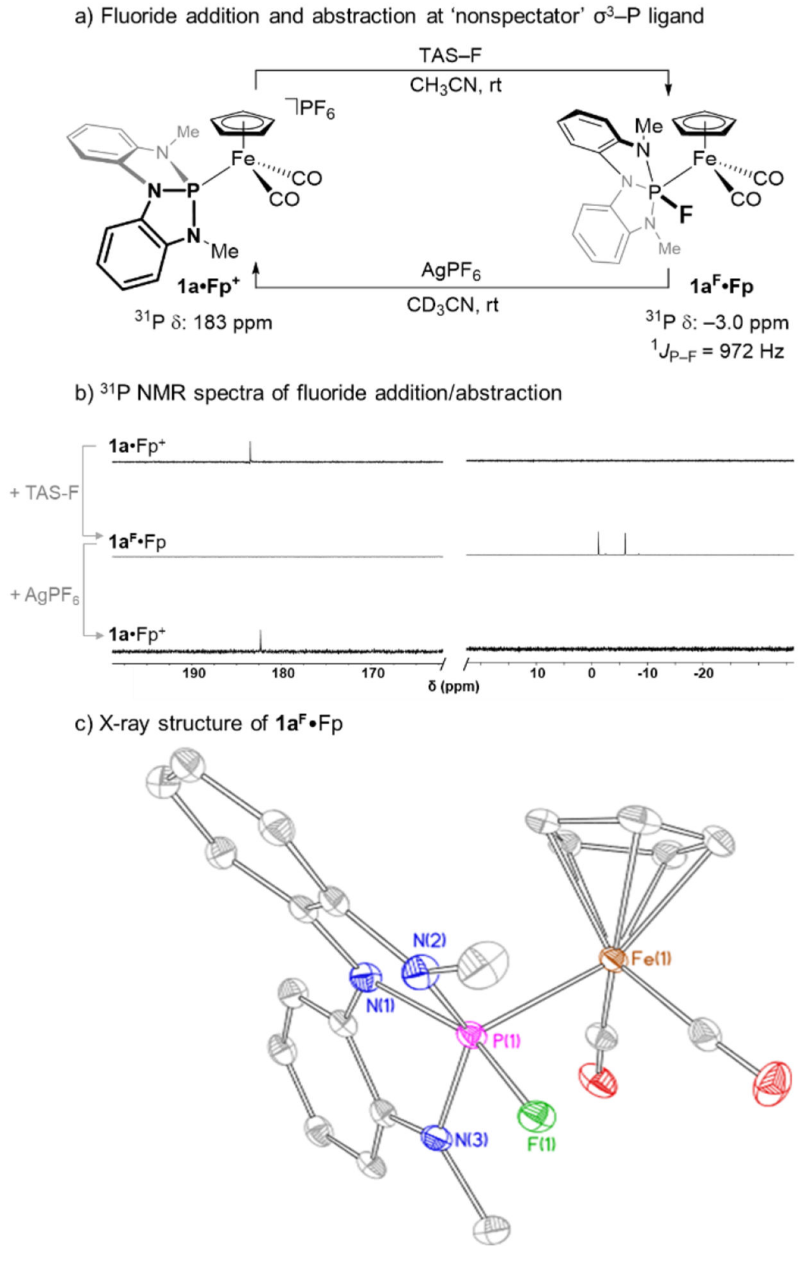

Figure 5.

A) Reversible fluorination of 1a•Fp^+ and the resulting fluorometallophosphorane $1a^F$•Fp. B) Solution ^{31}P NMR spectra in CD_3CN: (*top*) spectrum of 1a•Fp^+; (*middle*) spectrum of $1a^F$•Fp from addition of TASF to 1a•Fp^+; (*bottom*) spectrum of 1a•Fp^+ following treatment of $1a^F$•Fp with $AgPF_6$ and removal of precipitate (AgF). C) Thermal ellipsoid plot rendered at 50% probability level for $1a^F$•Fp. Hydrogen atoms are removed for clarity. Relevant metrical data for $1a^F$•Fp: d(Fe-P): 2.3047(9) Å, d(P-F): 1.6687(18) Å, $\angle(N_1\text{-P-F})$: 158.11(12)^o, $\angle(N_2\text{-P-}N_3)$: 134.91(13)^o, $\phi(C_2\text{-Fe-P-F}) = 2.63^o$, $\phi(C_1\text{-Fe-P-}N_3) = 8.12^o$. See SI for full details.

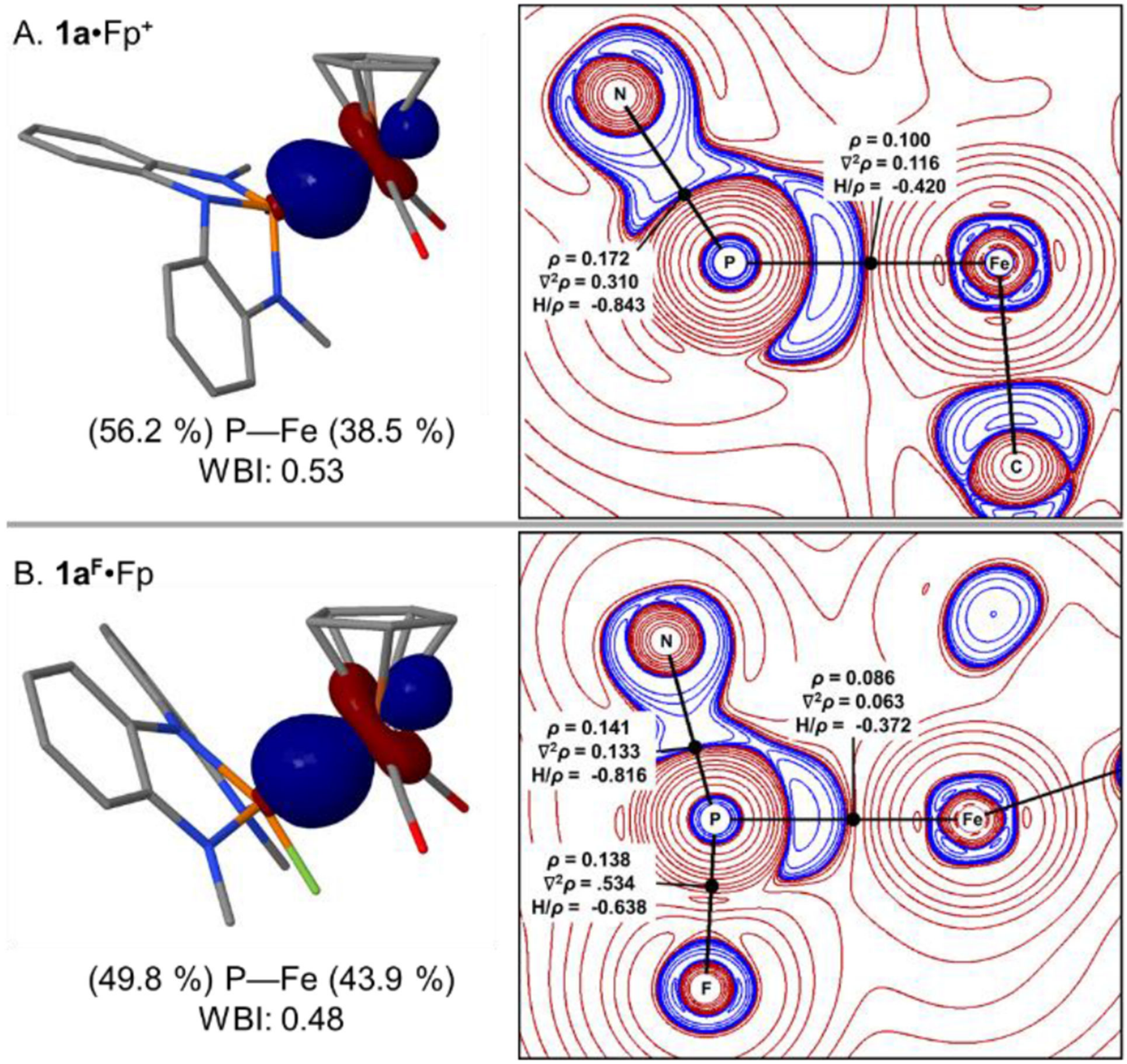

ionic contribution to the P–F bonding in **1a^{F}**•Fp.

Figure 6.

Bonding analysis for **1a**•Fp^{+} and **1a^{F}**•Fp. (A) *Left:* NLMO representing P–Fe bond for **1a**•Fp^{+}. *Right:* Contour plot of the Laplacian of the electron-density topology**1a**•Fp^{+} in the plane containing the Fe, P, and N atoms. Areas of charge depletion are depicted in red and areas of charge concentration are depicted in blue. Black dots indicate bond critical points. Metrics represent relevant properties at the bond critical points (ρ in e/Å^{3}, $\nabla^2\rho$ in e/Å^{5}, H/ρ in atomic units). (B) *Left:* NLMO representing P–Fe bond for **1a^{F}**•Fp. *Right:* Contour plot of the Laplacian of the electron-density topology **1a^{F}**•Fp in the plane containing the Fe, P, and F atoms.

Table 1.

Collected spectroscopic, structural, and computational data for compounds **1a**, **1b**, **1a**•Fp^+, **1b**•Fp^+, and **1a**^{F}•Fp.

Metric	^{31}P δ (ppm)[a]	$^{1}J_{P-Se}$ (Hz)	^{57}Fe δ (ppm)[b]	*d*(Fe_1-P_1) (Å)	ν(CO) (cm^{-1})	FIA (kcal/mol)[c]	EDA-NOCV[d]							
							E_{tot}	E_{Pauli}	E_{estat}	E_{steric}	E_{disp}	E_{orb}	σ(P→Fe)	π(P←Fe)
1a	160.4	907[e]	-	-	-	-	-	-	-	-	-	-	-	-
1b	122.4	784[e]	-	-	-	-	-	-	-	-	-	-	-	-
1a•Fp^+	183.5	-	616	2.1809(4)	2017, 2061	59.3	−91.9	122.7	−105.0	17.7	−16.1	−93.6	−61.7	−18.1
1b•Fp^+	141.4	-	688	2.2381(5)	2000, 2045	32.9	−99.8	130.0	−118.4	11.6	−18.4	−92.9	−65.8	−13.2
1a^F•Fp	−3.0	-	1013	2.3047(9)	1952, 2007	-	-	-	-	-	-	-	-	-

[a] ppm vs. 85% H_3PO_4.

[b] ppm vs. $Fe(CO)_5$.

[c] Computed (BP86/def2-TZVP(CPCM=CH_2Cl_2) according to the method in Ref. 32.

[d] EDA-NOCV computational results represent attractive and repulsive energies (kcal/mol) between the Fp^+ fragment and phosphorus ligands at the fragment geometry of the complex. The direction of donation is defined to be from phosphorus to iron.

[e] Values from Ref. 25.